Supporting Information for

Single-Crystals Syntheses and Properties of Indium-Organic Frameworks based on 1,1'-Ferrocenedicarboxylic Acid

Ran Gao[a,b], Shu-Mei Chen[a]*, Fei Wang[b]* and Jian Zhang[b]

[a]College of Chemistry, Fuzhou University, Fuzhou, Fujian 350108, China. E-mail: csm@fzu.edu.cn

[b]State Key Laboratory of Structural Chemistry, Fujian Institute of Research on the Structure of Matter, Chinese Academy of Sciences, Fuzhou, Fujian 350002, China. E-mail: wangfei04@fjirsm.ac.cn

Content

Expeimental Section

Materials and Physical Measurements. All the reagents and solvents were purchased commercially and were used as received without further purification. $InCl_3 \cdot 4H_2O$, 1,1'-ferrocenedicarboxylic acid, 2,2'-biimidazole, pyrazole, 4,4'-bipyridine, 3-nitro-1H-pyrazole, piperazine, tetrabutylammonium bromide and adenine were purchased from Adamas-beta. 2-methylimidazole, imidazole was acquired from Aladdin Chemical Reagent Shanghai. Ethanol (> 99.5%), ethylene glycol (> 99.5%) and NaOH were bought from Sinopharm Chemical Reagent Beijing. Fourier transform infrared spectroscopy (FTIR) data were collected on a PerkinElmer Spectrum 100 FT-IR spectrometer over a range 400−4000 cm^{-1}. The UV-vis diffuse reflection data were recorded at room temperature using a powder sample with $BaSO_4$ as a standard (100% reflectance) on a Perkin Elmer Lamda-950 UV spectrophotometer and scanned at 200−800 nm. The absorption data are calculated from the Kubelka-Munk function, $(F(R) = (1-R)^2/2R)$, where R representing the reflectance. The energy dispersive spectroscopy (EDS) analyses of single crystals were performed on a JEOL JSM6700F field-emission scanning electron microscope equipped with an Oxford INCA system. SEM was carried out on a field emission scanning electron microscope (FESEM, Phenom G2). Elemental analysis was measured on a Vario MICRO elemental analyzer instrument. Thermal stability studies were carried out on a NETZSCH STA-449C thermal analyzer with a heating rate of 10 °C/min under a nitrogen atmosphere. Powder X-ray diffraction (PXRD) data were collected on a Rigaku Mini Flex II diffractometer using Cu−Kα radiation (λ = 1.54056 Å) under ambient conditions. Gas adsorption measurement was performed in the ASAP (Accelerated Surface Area and Porosimetry) 2020 system.

Care should be taken when handling glass reactors after synthesis, as the pressure increase is significant, even after cooling to room temperature due to the decomposition of the reactants and solvents during the reaction. This results in a strong smelling gas mixture which should be released under a fume hood with good ventilation. Moreover, 1,1'-ferrocenedicarboxylic acid is irritating to the eyes, respiratory tract and skin, so personal protection should be taken when using it.

Single-Crystal X-ray Diffraction Studies: Crystallographic data for 1-7 were collected on a Supernova single-crystal diffractometer equipped with graphite-monochromatized CuKα or GaKα radiation (λ = 1.54056 or 1.3405, respectively) at 100 K. Absorption corrections were applied using *SADABS*. The structures were solved by the direct method and refined by full-matrix least-squares on F^2 using *SHELXTL*. In these structures, some cations and free solvent molecules were highly disordered and could not be located. The diffused electron densities resulting from these residual cations and solvent molecules were removed from the data set using the SQUEEZE routine of *PLATON* and refined further using the data generated. Crystal data and details of 1-7 are summarized in Table 1. CCDC 2026158−2026164 entries contain the supplementary crystallographic data for this paper. These data can be obtained free of charge from the Cambridge Crystallographic Data Centre.

Cyclic Voltammetric Experiments The working electrodes were prepared by the solution coating method. The new prepared samples (8 mg) and nafion (30 μL) were dissolved in 1 mL ethanol and 6 mL H_2O. Then sonicated and dripped the 60 μL solution evenly on the cleaned FTO conductive glass (1.0 × 4.0 cm^2 , 50 Ω per square cm) to obtain the coating film. The cyclic voltammetric experiments were performed on a CHI760E electrochemistry workstation in a three-electrode system, with a Pt plate as the counter electrode and an Ag/AgCl electrode as the reference electrode. The experiments were performed at room temperature in 0.01 M $NaPF_6$ /acetonitrile electrolyte. The CV cycles were measured with a scan rate of 50 mV s^{-1}.

Photocurrent Measurement The working electrodes were prepared by the solution coating method. The new prepared samples (5 mg) and nafion (10 μL) were dissolved in 0.5 mL ethanol, then sonicated and dripped the 40 μL solution evenly on the cleaned FTO conductive glass (1.0 × 4.0 cm^2 , 50 Ω per square cm) to obtain the coating film. The photocurrent experiments were performed on a CHI760E electrochemistry workstation in a three-electrode system, with a Pt plate as the counter electrode and an Ag/AgCl electrode as the reference electrode. The experiments were performed at room temperature in 0.2 M Na_2SO_4 electrolyte and a 300 W high pressure xenon lamp was used as a visible light source. In order to eliminate the error caused by the uneven film thickness, the backside illumination method was used to solve it. During the testing process, the lamp was kept on continuously. A manual shutter was used to block exposure of the sample to the light.

1. Single crystal images of 1-7.

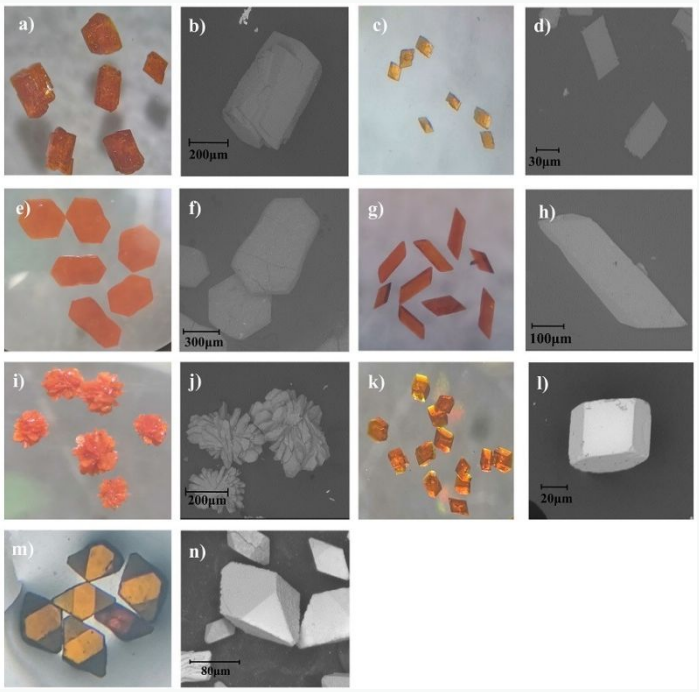

Figure S1. The optical micrographs and SEM photographs of crystals 1-7 (a-n).

2. Structure

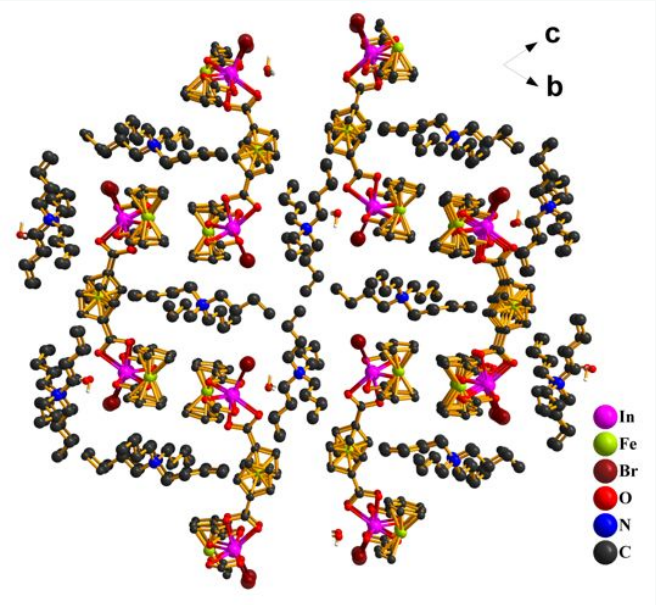

Fig S2. The packing structure of 1 along a-axis.

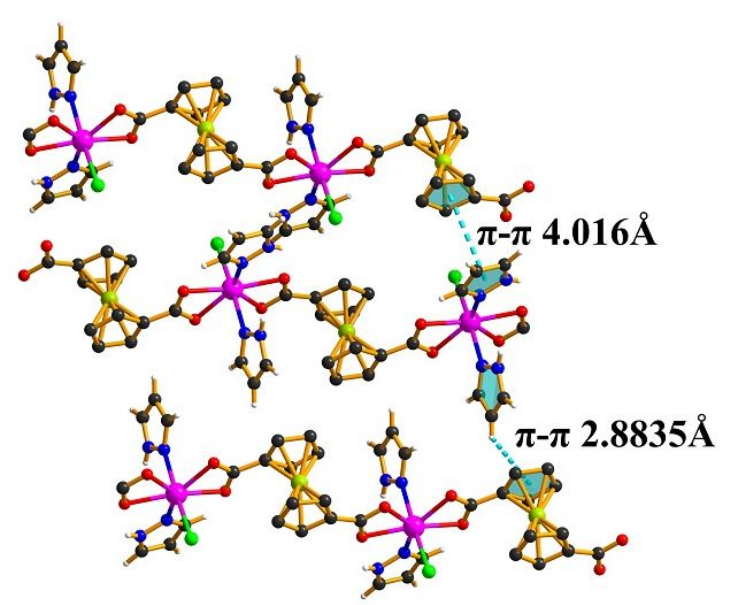

Fig S3. The π-π interactions between adjacent different chains in 2.

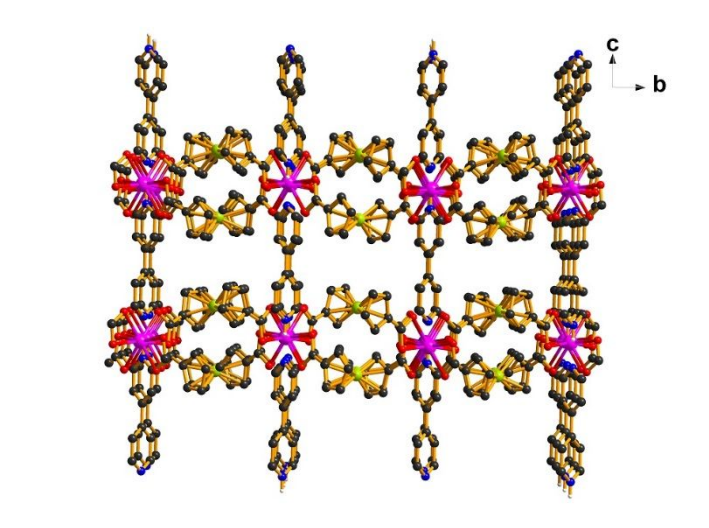

Fig S4. The packing structure of 3 along a-axis.

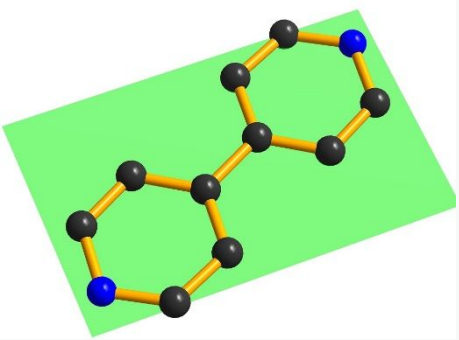

Fig S5. The orientation of the pyridine groups in the 4,4'-bipyridine molecules in 4.

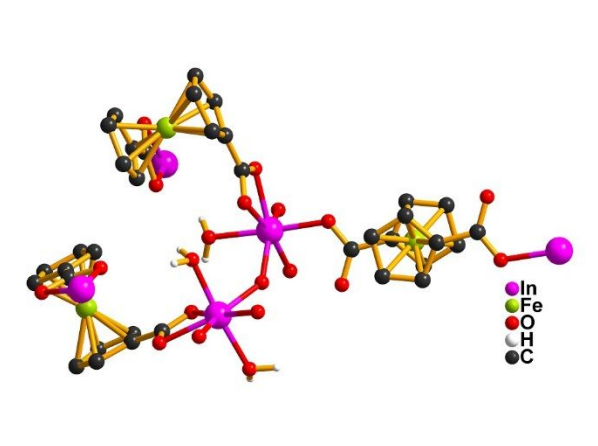

Fig S6. The coordination environment of In(III) ion in 5.

3. Hydrogen bond parameters and selected bond lengths (Å) and angles (°) for 1-7.

Table S1. Selected bond lengths (Å) and angles (°) for **1.**

In1-Br2	2.5150 (14)	O5-In1-O2^{i}	142.18 (19)

In1-O6	2.259 (5)	O5-In1-O4	57.50 (19)
In1-O7	2.234 (5)	O2^{i}-In1-Br2	89.20 (14)
In1-O3^{i}	2.239 (5)	O2^{i}-In1-O4	160.03 (19)
In1-O5	2.220 (5)	O4-In1-Br2	89.91 (14)
In1-O2^{i}	2.305 (5)	O11-In2-Br1	96.36 (14)
In1-O4	2.341 (5)	O11-In2-O12^{ii}	144.25 (19)
In2-Br1	2.5203 (14)	O11-In2-O9	89.3 (2)
In2-O11	2.205 (5)	O11-In2-O13^{ii}	86.48 (19)
In2-O12^{ii}	2.303 (5)	O11-In2-O10	57.92 (19)
In2-O9	2.240 (5)	O11-In2-O8	128.43 (19)
In2-O13^{ii}	2.243 (5)	O12^{ii}-In2-Br1	90.56 (14)
In2-O10	2.331 (5)	O12^{ii}-In2-O10	157.75 (19)
In2-O8	2.287 (5)	O9-In2-Br1	169.58 (14)
O6-In1-Br2	104.26 (14)	O9-In2-O12^{ii}	89.92 (19)
O6-In1-O2^{i}	80.42 (19)	O9-In2-O13^{ii}	88.98 (19)
O6-In1-O4	80.47 (18)	O9-In2-O10	88.36 (19)
O7-In1-Br2	162.71 (15)	O9-In2-O8	57.93 (19)
O7-In1-O6	58.5 (2)	O13^{ii}-In2-Br1	100.06 (15)
O7-In1-O3^{i}	92.2 (2)	O13^{ii}-In2-O12^{ii}	57.8 (2)
O7-In1-O2^{i}	88.03 (19)	O13^{ii}-In2-O10	144.32 (19)
O7-In1-O4	86.92 (19)	O13^{ii}-In2-O8	126.62 (19)
O3^{i}-In1-Br2	100.76 (15)	O10-In2-Br1	87.26 (14)
O3^{i}-In1-O6	130.50 (19)	O8-In2-Br1	111.97 (14)
O3^{i}-In1-O2^{i}	57.85 (19)	O8-In2-O12^{ii}	79.72 (19)
O3^{i}-In1-O4	141.65 (19)	O8-In2-O10	80.60 (18)
O5-In1-Br2	99.26 (14)	O5-In1-O2^{i}	142.18 (19)
O5-In1-O6	131.4 (2)	O5-In1-O4	57.50 (19)
O5-In1-O7	93.3 (2)	O2^{i}-In1-Br2	89.20 (14)
O5-In1-O3^{i}	84.3 (2)	O2^{i}-In1-O4	160.03 (19)

Symmetry codes: (i) x−1, y, z; (ii) x+1, y, z.

Table S2. Selected bond lengths (Å) and angles (°) for **2.**

In1-Cl1	2.4573 (10)	O3^{i}-In1-O1	160.00 (11)
In1-O1	2.283 (3)	O3^{i}-In1-O4^{i}	57.83 (10)
In1-O2	2.248 (3)	O3^{i}-In1-N1	88.25 (11)
In1-O3^{i}	2.271 (3)	O4^{i}-In1-Cl1	90.36 (7)
In1-O4^{i}	2.274 (3)	O4^{i}-In1-O1	141.62 (10)
In1-N3	2.243 (3)	N3-In1-Cl1	97.78 (9)
In1-N1	2.274 (3)	N3-In1-O1	81.79 (11)
O1-In1-Cl1	91.30 (7)	N3-In1-O2	138.65 (11)
O2-In1-Cl1	93.16 (7)	N3-In1-O3^{i}	78.32 (12)
O2-In1-O1	58.12 (10)	N3-In1-O4^{i}	135.83 (11)
O2-In1-O3^{i}	140.77 (10)	N3-In1-N1	87.16 (12)

O2-In1-O4^{i}	83.51 (10)	N1-In1-Cl1	175.01 (9)
O2-In1-N1	82.60 (11)	N1-In1-O1	88.70 (11)
O3^{i}-In1-Cl1	93.43 (8)	N1-In1-O4^{i}	86.55 (11)

Symmetry codes: (i) *x*, *y*+1, *z*; (ii) *x*, *y*−1, *z*.

Table S3. Selected bond lengths (Å) and angles (°) for **3.**

In1-O1	2.318 (8)	O3^{ii}-In1-O1	85.6 (3)
In1-O1^{i}	2.318 (8)	O3^{ii}-In1-O1^{i}	95.4 (3)
In1-O4^{ii}	2.265 (7)	O3^{iii}-In1-O1^{i}	85.6 (3)
In1-O4^{iii}	2.265 (7)	O3^{iii}-In1-O1	95.4 (3)
In1-O3^{ii}	2.262 (8)	O3^{ii}-In1-O4^{iii}	133.1 (4)
In1-O3^{iii}	2.262 (8)	O3^{iii}-In1-O4^{iii}	56.9 (3)
In1-O2^{i}	2.293 (7)	O3^{iii}-In1-O4^{ii}	133.1 (4)
In1-O2	2.293 (7)	O3^{ii}-In1-O4^{ii}	56.9 (3)
O1-In1-O1^{i}	168.4 (5)	O3^{ii}-In1-O3^{iii}	170.0 (6)
O4^{iii}-In1-O1	88.5 (3)	O3^{iii}-In1-O2^{i}	86.3 (3)
O4^{ii}-In1-O1	82.4 (3)	O3^{ii}-In1-O2	86.3 (3)
O4^{ii}-In1-O1^{i}	88.5 (3)	O3^{ii}-In1-O2^{i}	86.0 (3)
O4^{iii}-In1-O1^{i}	82.4 (3)	O3^{iii}-In1-O2	86.0 (3)
O4^{iii}-In1-O4^{ii}	76.2 (4)	O2^{i}-In1-O1^{i}	56.5 (3)
O4^{ii}-In1-O2	127.5 (3)	O2^{i}-In1-O1	135.1 (3)
O4^{iii}-In1-O2^{i}	127.5 (3)	O2-In1-O1^{i}	135.1 (3)
O4^{iii}-In1-O2	127.3 (3)	O2-In1-O1	56.5 (3)
O4^{ii}-In1-O2^{i}	127.3 (3)	O2^{i}-In1-O2	79.0 (4)

Symmetry codes: (i) −*x*, −*y*+1, *z*; (ii) −*x*+1/2, *y*+1/2, −*z*+2; (iii) *x*−1/2, −*y*+1/2, −*z*+2; (iv) −*x*+1, −*y*+1, *z*; (v) −*x*+1/2, *y*−1/2, −*z*+2.

Table S4. Hydrogen bond parameters for **3**.

D-H-A	d(D-H)	d(D-A)	d(H-A)	<(DHA)
N(1)-H(1)-N(2)^{i}	0.86	2.623(14)	1.76	180

Symmetry codes: (i) x, y, -1+z.

Table S5. Selected bond lengths (Å) and angles (°) for **4.**

In1-O3	2.250 (5)	O1-In1-O3	83.90 (17)
In1-O6^{i}	2.271 (5)	O1-In1-O6^{i}	87.48 (18)
In1-O7^{i}	2.353 (5)	O1-In1-O7^{i}	99.00 (18)
In1-O1	2.188 (5)	O1-In1-O2	79.96 (19)
In1-O2	2.325 (5)	O1-In1-N1	82.8 (2)
In1-N1	2.281 (6)	O2-In1-O7^{i}	166.59 (18)
In1-O4	2.067 (7)	N1-In1-O7^{i}	81.84 (19)
O3-In1-O6^{i}	80.55 (17)	N1-In1-O2	84.77 (18)
O3-In1-O7^{i}	136.44 (18)	O4-In1-O3	100.8 (3)

O3-In1-O2	56.93 (17)	O4-In1-O6^{i}	106.7 (3)
O3-In1-N1	141.09 (17)	O4-In1-O7^{i}	87.0 (2)
O6^{i}-In1-O7^{i}	56.37 (18)	O4-In1-O1	165.6 (3)
O6^{i}-In1-O2	136.51 (17)	O4-In1-O2	91.1 (2)
O6^{i}-In1-N1	134.90 (19)	O4-In1-N1	85.1 (3)

Symmetry codes: (i) −x+1, −y+1, −z+1; (ii) −x, −y+1, −z; (iii) −x+1, −y+2, −z.

Table S6. Selected bond lengths (Å) and angles (°) for **5.**

In1-O14^{i}	2.234 (5)	O13-In1-O12	56.37 (16)
In1-O5	2.083 (5)	O13-In1-O15^{i}	136.09 (17)
In1-O4	2.132 (5)	O15^{i}-In1-O12	166.89 (16)
In1-O12	2.439 (5)	O16-In1-O14^{i}	85.74 (19)
In1-O13	2.204 (5)	O16-In1-O12	84.70 (18)
In1-O15^{i}	2.342 (5)	O16-In1-O13	84.61 (19)
In1-O16	2.190 (5)	O16-In1-O15^{i}	92.10 (18)
In2-O5	2.080 (5)	O5-In2-O8	86.08 (19)
In2-O8	2.186 (5)	O5-In2-O7	142.07 (19)
In2-O7	2.181 (6)	O5-In2-O11^{ii}	138.3 (2)
In2-O11^{ii}	2.312 (5)	O5-In2-O10^{ii}	82.22 (19)
In2-O10^{ii}	2.297 (5)	O5-In2-O6	84.50 (19)
In2-O6	2.318 (6)	O5-In2-O2	93.1 (2)
In2-O2	2.166 (6)	O8-In2-O11^{ii}	93.60 (17)
O14^{i}-In1-O12	135.59 (16)	O8-In2-O10^{ii}	91.6 (2)
O14^{i}-In1-O15^{i}	56.48 (16)	O8-In2-O6	89.7 (2)
O5-In1-O14^{i}	139.46 (19)	O7-In2-O8	86.72 (18)
O5-In1-O4	96.60 (19)	O7-In2-O11^{ii}	79.35 (18)
O5-In1-O12	82.29 (18)	O7-In2-O10^{ii}	135.20 (17)
O5-In1-O13	137.95 (19)	O7-In2-O6	58.26 (18)
O5-In1-O15^{i}	84.74 (19)	O11^{ii}-In2-O6	137.23 (19)
O5-In1-O16	84.2 (2)	O10^{ii}-In2-O11^{ii}	56.05 (18)
O4-In1-O14^{i}	95.66 (18)	O10^{ii}-In2-O6	166.53 (18)
O4-In1-O12	92.19 (17)	O2-In2-O8	170.9 (2)
O4-In1-O13	92.62 (18)	O2-In2-O7	88.4 (2)
O4-In1-O15^{i}	91.22 (18)	O2-In2-O11^{ii}	93.0 (2)
O4-In1-O16	176.64 (18)	O2-In2-O10^{ii}	97.2 (3)
O13-In1-O14^{i}	79.61 (17)	O2-In2-O6	81.3 (3)

Symmetry codes: (i) −x, −y, −z+1; (ii) −x+1, −y+1, −z+1; (iii) −x, −y+1, −z+2.

Table S7. Hydrogen bond parameters for **5**.

D-H-A	d(D-H)	d(D-A)	d(H-A)	<(DHA)
O(1)-H(1A)-O(3)	0.85	3.143(10)	2.48	135
O(1)-H(1B)-O(10)^{i}	0.85	3.063(11)	2.22	173

O(2)-H(2A)-O(1)	0.95	2.734(11)	1.80	169
O(2)-H(2B)-O(3)^{ii}	0.94	2.683(9)	1.93	135
O(5)-H(5)-O(3)	0.72(7)	2.786(9)	2.13(8)	152(3)
O(8)-H(8A)-O(11)	0.85	2.732(9)	2.02	141
O(8)-H(8A)-O(7)^{iii}	0.85	3.205(8)	2.51	140
O(8)-H(8B)-O(16)	0.85	3.196(8)	2.47	143
O(16)-H(16A)-O(10)^{iii}	0.87	2.668(8)	2.04	128
O(16)-H(16B)-O(14)	0.86	2.664(8)	2.01	132

Symmetry codes: (i) -1+x, y, z (ii) -x, 1-y, 1- z (iii) 1-x, 1-y, 1- z.

Table S8. Selected bond lengths (Å) and angles (°) for **6.**

In1-Cl1	2.4107 (5)	O4^{i}-In1-Cl1	102.55 (4)
In1-O4^{i}	2.1803 (14)	O4^{i}-In1-O5^{i}	57.73 (5)
In1-O5^{i}	2.3478 (16)	O4^{i}-In1-N2	143.77 (6)
In1-O2	2.1626 (15)	O4^{i}-In1-N4	94.52 (6)
In1-N2	2.2350 (17)	O5^{i}-In1-Cl1	96.19 (4)
In1-N4	2.2466 (18)	O2-In1-Cl1	91.75 (4)
N2-In1-Cl1	91.62 (5)	O2-In1-O4^{i}	82.94 (6)
N2-In1-O5^{i}	87.99 (6)	O2-In1-O5^{i}	140.67 (6)
N2-In1-N4	73.68 (6)	O2-In1-N2	130.33 (6)
N4-In1-Cl1	162.90 (5)	O2-In1-N4	91.30 (6)
N4-In1-O5^{i}	92.07 (6)		

Symmetry code: (i) $-x+1, -y+1, -z+1$.

Table S9. Hydrogen bond parameters for **6**.

D-H-A	d(D-H)	d(D-A)	d(H-A)	<(DHA)
N(1)-H(1)-O(3)^{i}	0.86	2.864(3)	2.01	170
O(1)-H(1B)-O(2)^{ii}	0.85	3.057(2)	2.25	158
O(1)-H(1C)-O(3)^{i}	0.85	2.933(2)	2.13	157
N(3)-H(3)-O(1)	0.86	2.719(3)	1.89	162

Symmetry codes: (i)1-x, 1-y, -z (ii) 1-x, 1/2+y, 1/2-z

Table S10. Selected bond lengths (Å) and angles (°) for **7.**

In1-O6	2.080 (6)	O7^{i}-In1-O7	180.0
In1-O6^{i}	2.080 (6)	O5^{iv}-In3-O5	180.0
In1-O2^{ii}	2.166 (6)	O5^{iv}-In3-O9^{vi}	93.5 (2)
In1-O2^{iii}	2.166 (6)	O5-In3-O9^{v}	93.5 (2)
In1-O7^{i}	2.155 (6)	O5-In3-O9^{vi}	86.5 (2)
In1-O7	2.155 (6)	O5^{iv}-In3-O9^{v}	86.5 (2)
In3-O5	2.105 (6)	O5-In3-O3	92.3 (2)
In3-O5^{iv}	2.105 (6)	O5^{iv}-In3-O3	87.7 (2)

In3-O9^{v}	2.172 (6)	O5-In3-O3^{iv}	87.7 (2)
In3-O9^{vi}	2.172 (6)	O5^{iv}-In3-O3^{iv}	92.3 (2)
In3-O3	2.176 (7)	O9^{v}-In3-O9^{vi}	180.0 (5)
In3-O3^{iv}	2.176 (7)	O9^{vi}-In3-O3^{iv}	92.8 (3)
In2-O5	2.078 (6)	O9^{vi}-In3-O3	87.2 (3)
In2-O6	2.096 (6)	O9^{v}-In3-O3^{iv}	87.2 (3)
In2-O1^{iii}	2.161 (6)	O9^{v}-In3-O3	92.8 (3)
In2-O4	2.149 (6)	O3^{iv}-In3-O3	180.0
In2-O10^{v}	2.165 (6)	O5-In2-O6	172.8 (2)
In2-O8^{i}	2.175 (6)	O5-In2-O1^{iii}	94.1 (2)
O6-In1-O6^{i}	180.00 (17)	O5-In2-O4	91.1 (2)
O6-In1-O2^{ii}	89.7 (2)	O5-In2-O10^{v}	90.3 (3)
O6^{i}-In1-O2^{ii}	90.3 (2)	O5-In2-O8^{i}	89.3 (2)
O6^{i}-In1-O2^{iii}	89.7 (2)	O6-In2-O1^{iii}	91.4 (2)
O6-In1-O2^{iii}	90.3 (2)	O6-In2-O4	83.2 (2)
O6-In1-O7^{i}	91.3 (3)	O6-In2-O10^{v}	85.5 (3)
O6^{i}-In1-O7^{i}	88.7 (3)	O6-In2-O8^{i}	95.3 (2)
O6-In1-O7	88.7 (3)	O1^{iii}-In2-O10^{v}	85.8 (3)
O6^{i}-In1-O7	91.3 (3)	O1^{iii}-In2-O8^{i}	90.1 (3)
O2^{iii}-In1-O2^{ii}	180.0 (4)	O4-In2-O1^{iii}	174.5 (2)
O7^{i}-In1-O2^{iii}	89.5 (2)	O4-In2-O10^{v}	92.4 (3)
O7-In1-O2^{iii}	90.5 (2)	O4-In2-O8^{i}	91.7 (3)
O7^{i}-In1-O2^{ii}	90.5 (2)	O10^{v}-In2-O8^{i}	175.8 (3)
O7-In1-O2^{ii}	89.5 (2)		

Symmetry codes: (i) −*x*+1, −*y*, −*z*+1; (ii) −*x*+1, −*y*+1, −*z*+1; (iii) *x*, *y*−1, *z*; (iv) −*x*+1, −*y*, −*z*; (v) −*x*+2, −*y*, −*z*+1; (vi) *x*−1, *y*, *z*−1; (vii) *x*, *y*+1, *z*; (viii) *x*+1, *y*, *z*+1.

4. PXRD analyses for 1-7.

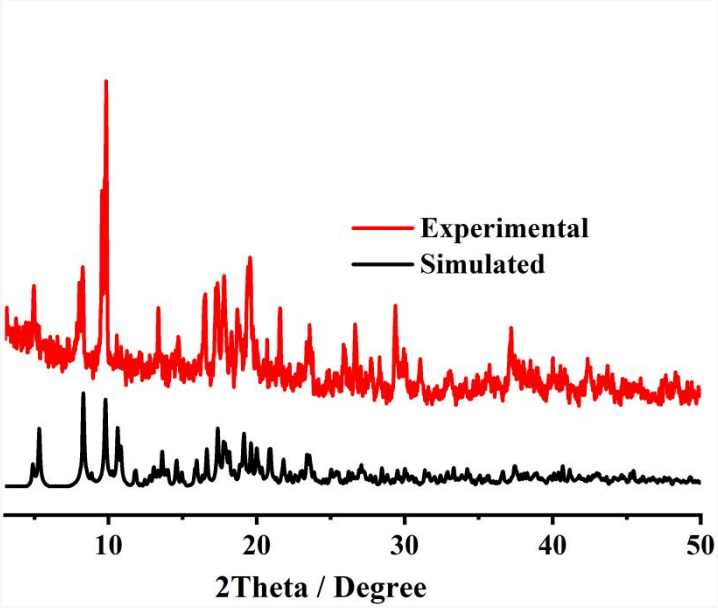

Figure S7. The PXRD of the simulated, experimental patterns of 1.

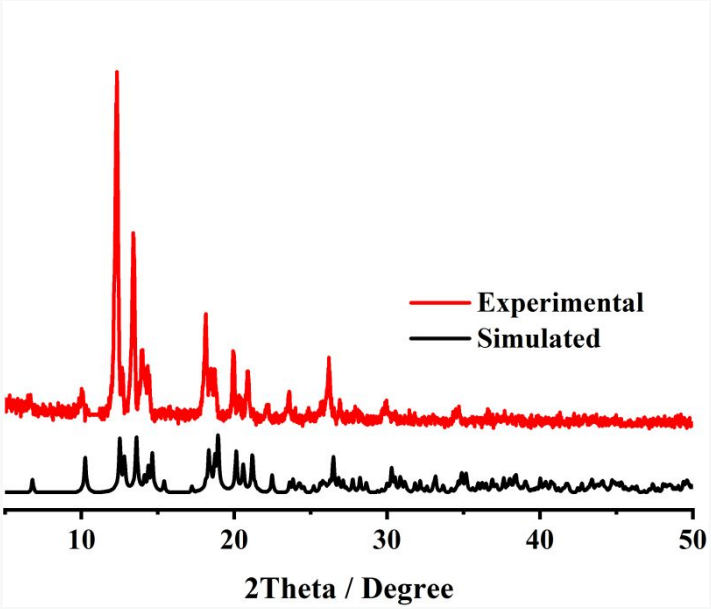

Figure S8. The PXRD of the simulated, experimental patterns of 2.

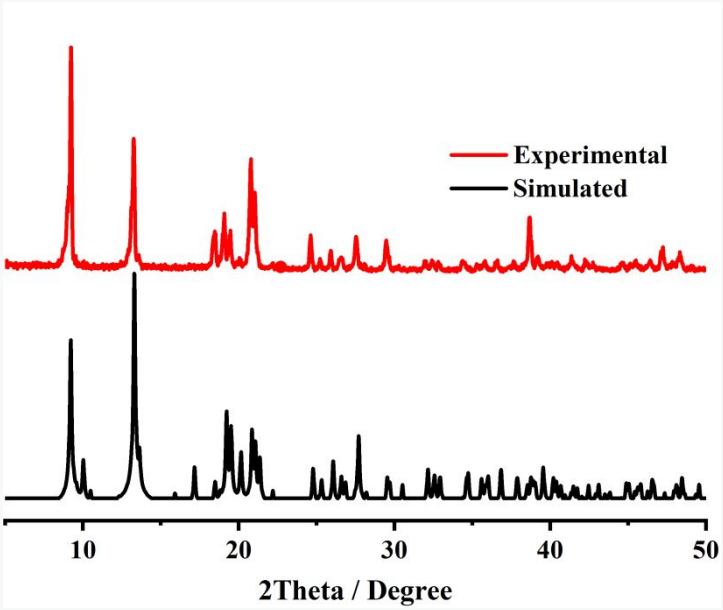

Figure S9. The PXRD of the simulated, experimental patterns of 3.

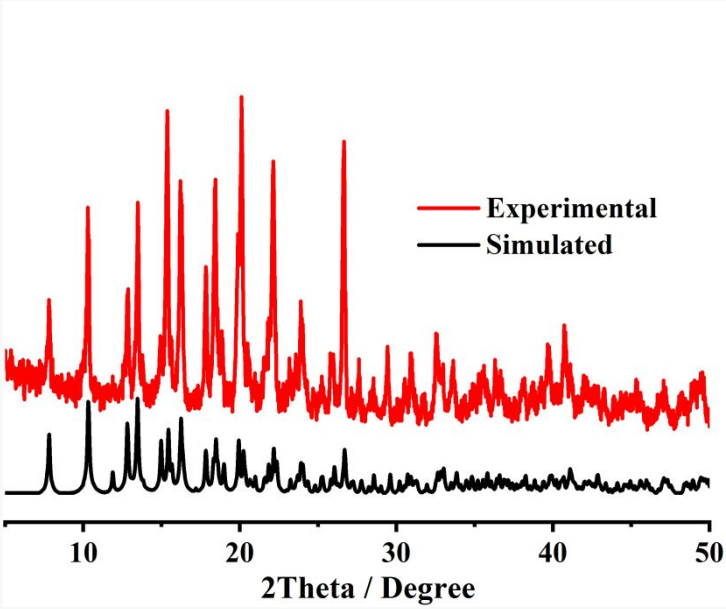

Figure S10. The PXRD of the simulated, experimental patterns of 4.

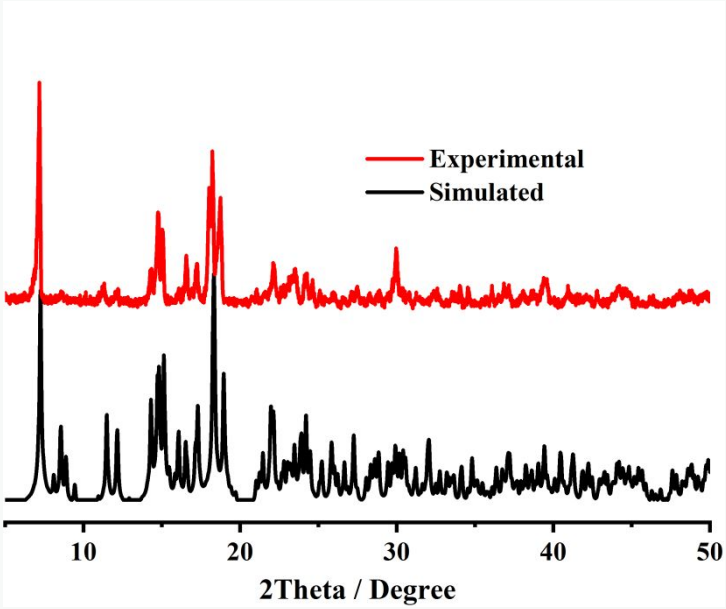

Figure S11. The PXRD of the simulated, experimental patterns of 5.

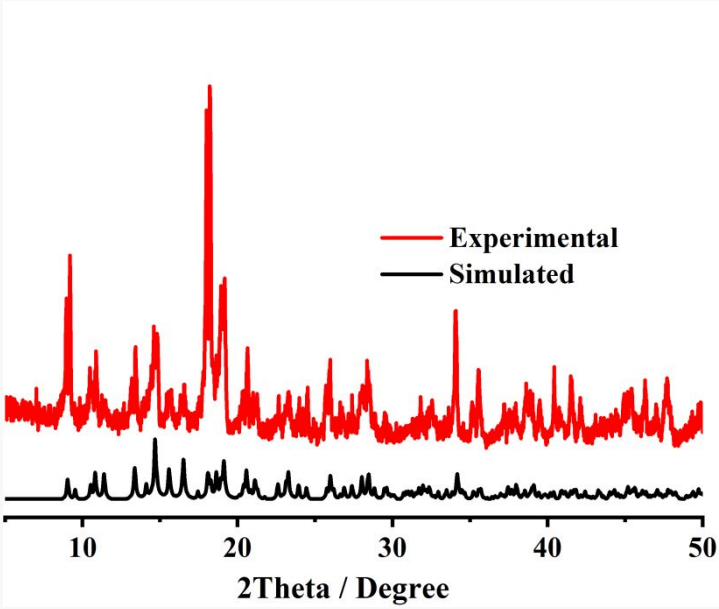

Figure S12. The PXRD of the simulated, experimental patterns of 6.

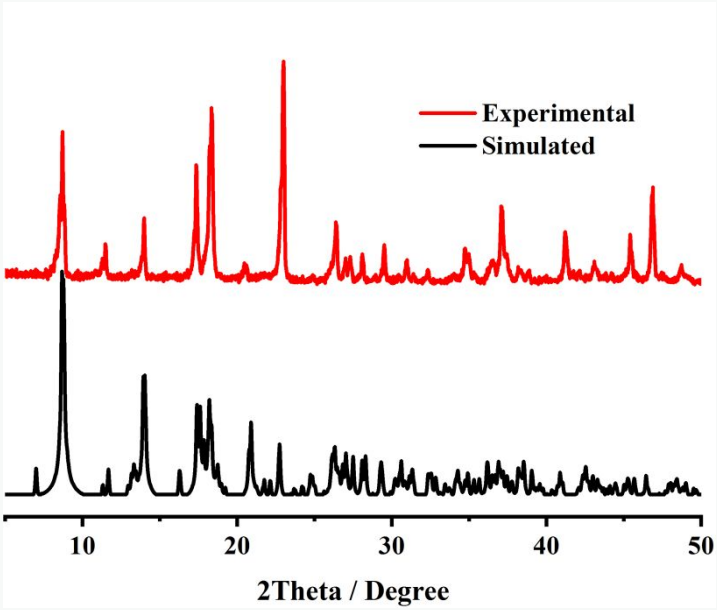

Figure S13. The PXRD of the simulated, experimental patterns of 7.

5. EDS spectra of 1-7.

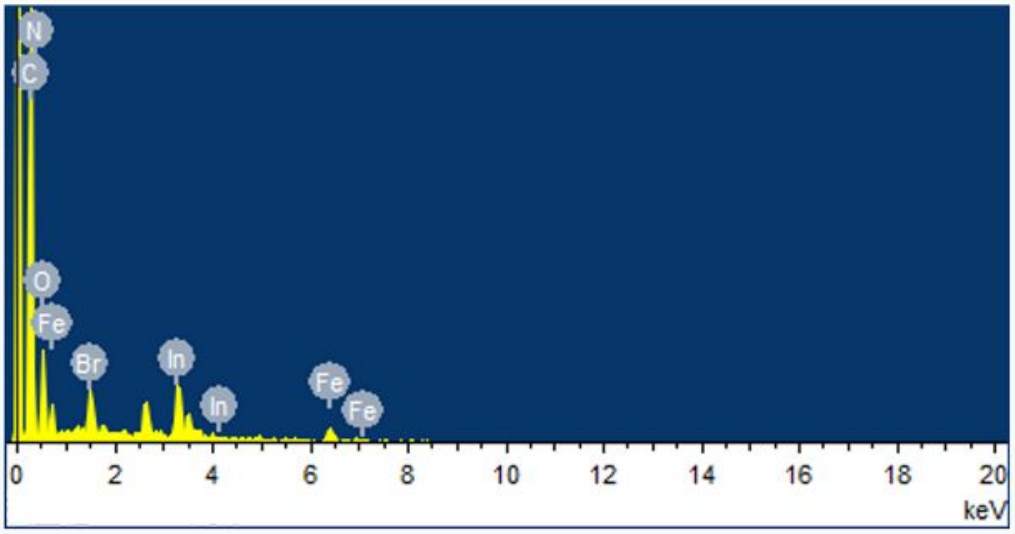

Figure S14. The EDS spectrum of 1.

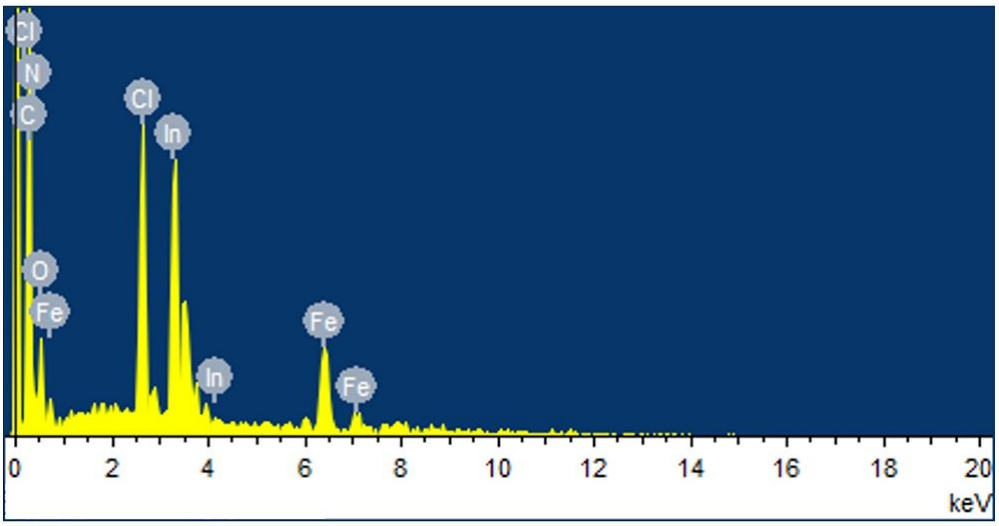

Figure S15. The EDS spectrum of 2.

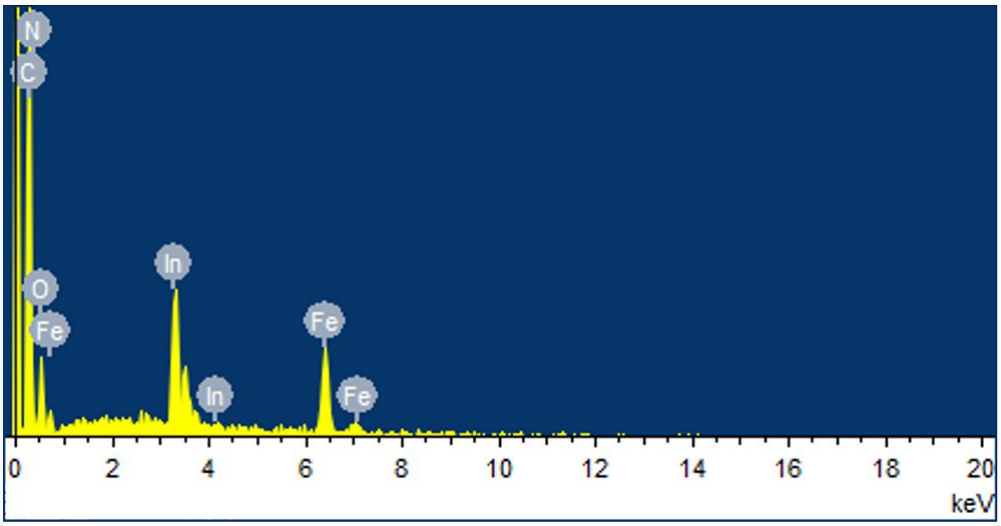

Figure S16. The EDS spectrum of 3.

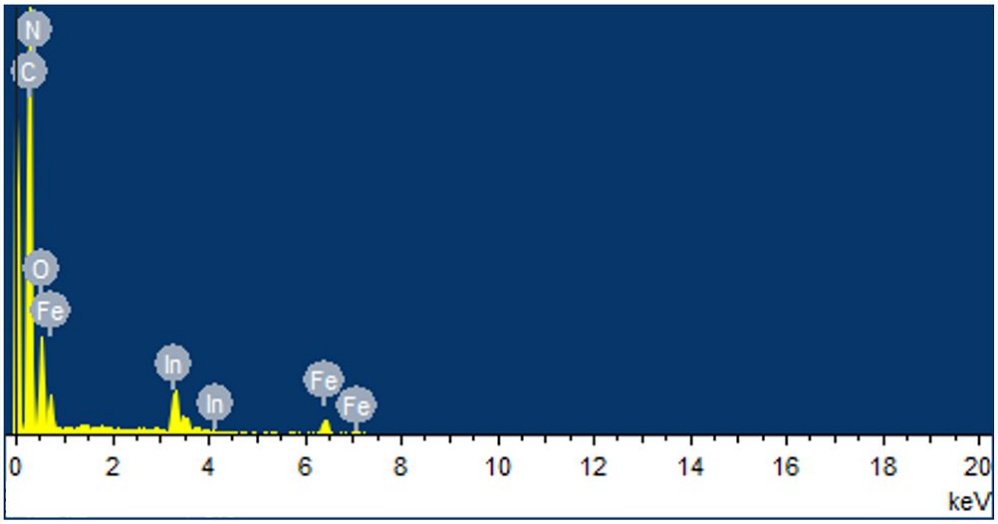

Figure S17. The EDS spectrum of 4.

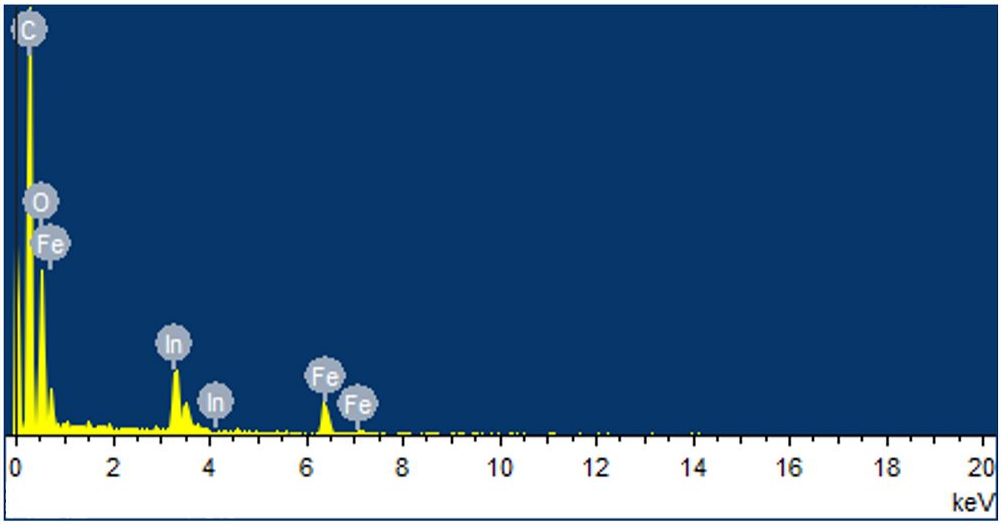

Figure S18. The EDS spectrum of 5.

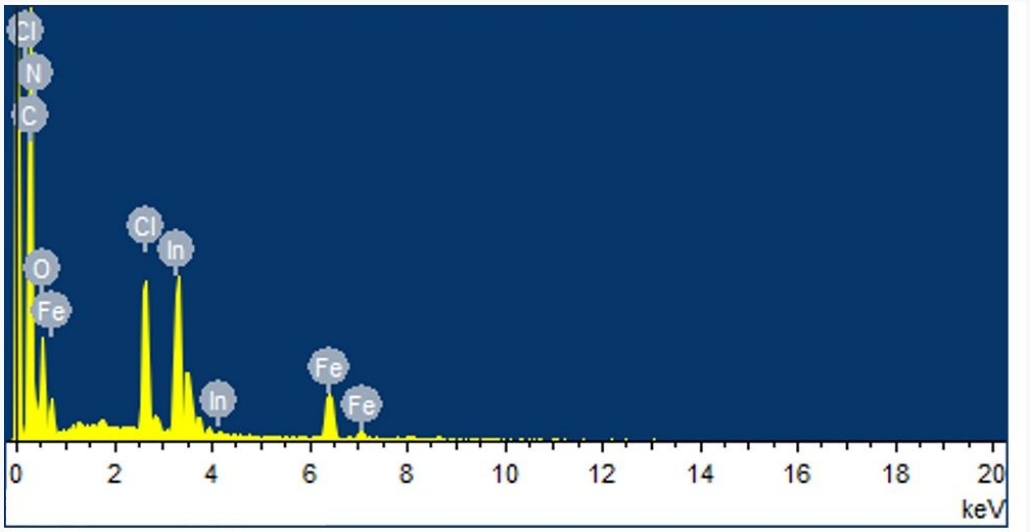

Figure S19. The EDS spectrum of 6.

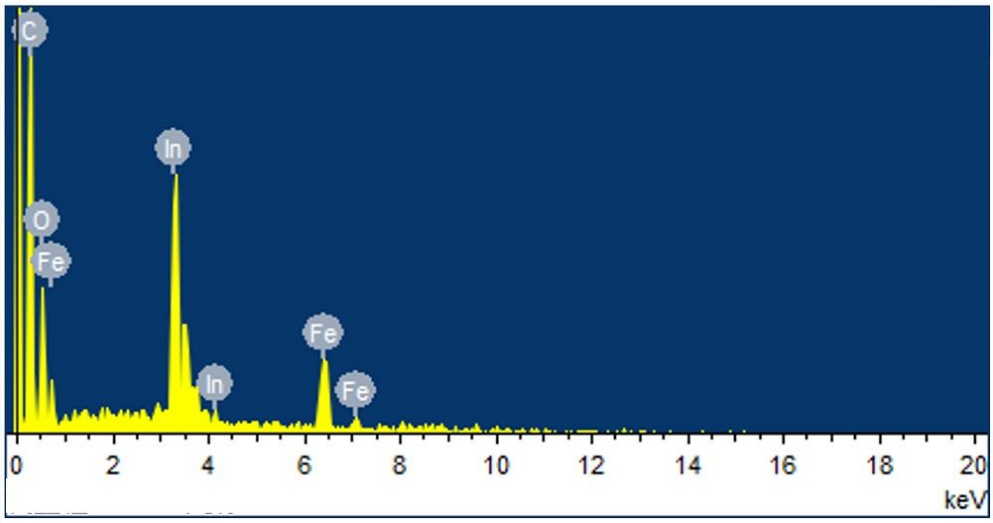

Figure S20. The EDS spectrum of 7.

6. TGA curves of 1-7.

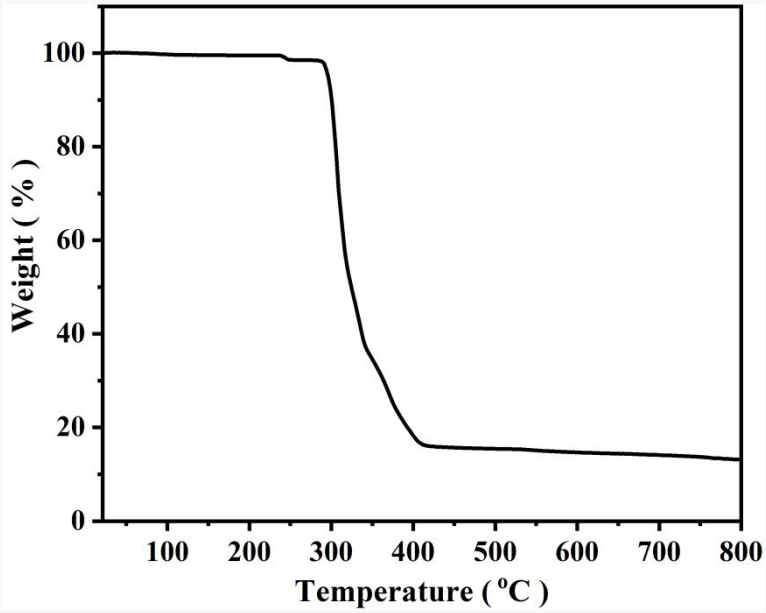

Figure S21. The TGA curve for 1.

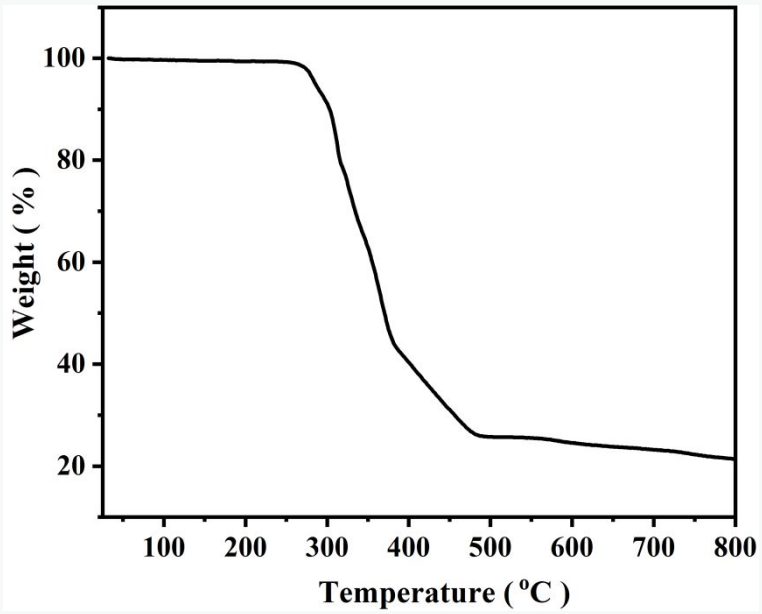

Figure S22. The TGA curve for 2.

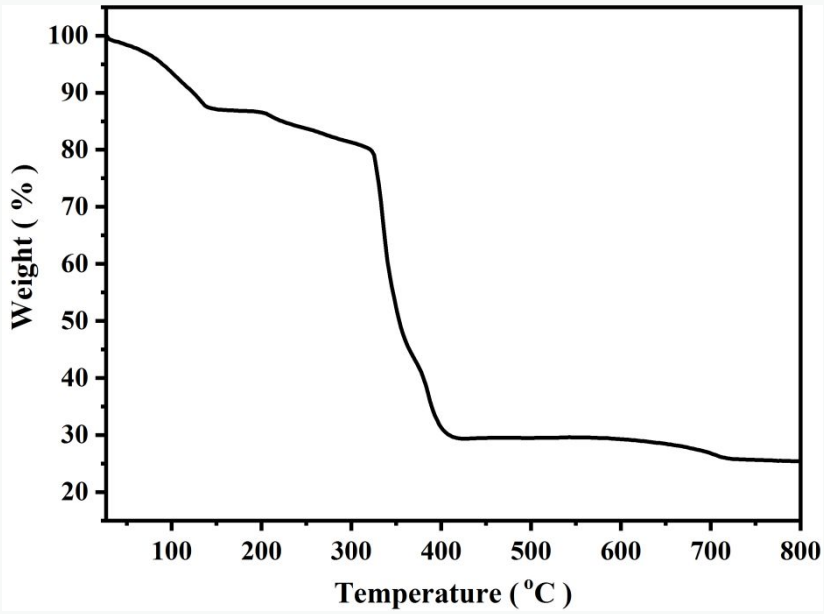

Figure S23. The TGA curve for 3.

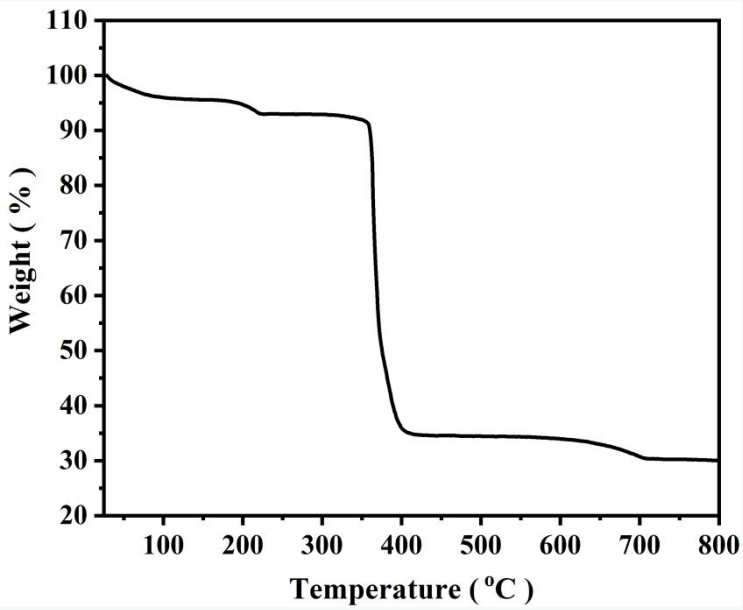

Figure S24. The TGA curve for 4.

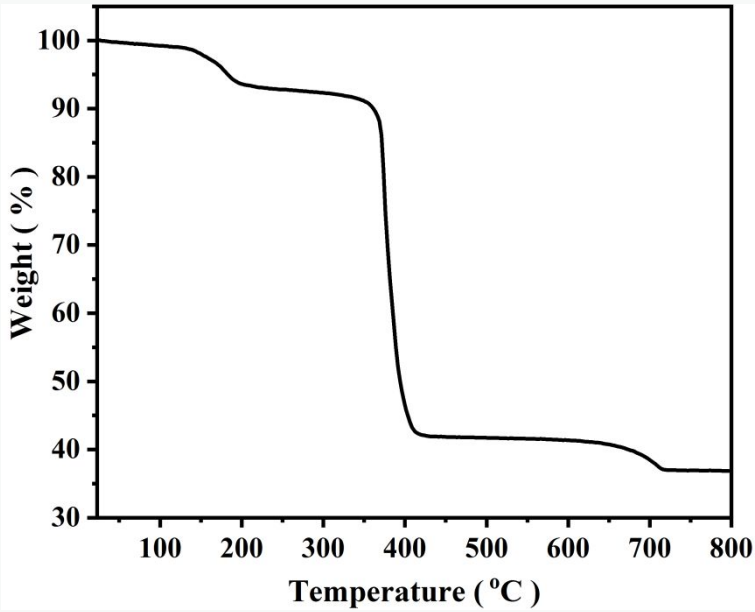

Figure S25. The TGA curve for 5.

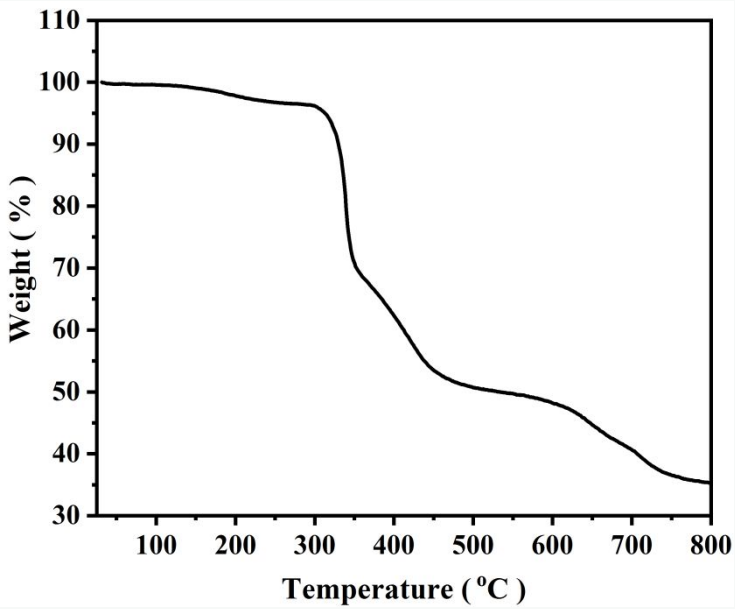

Figure S26. The TGA curve for 6.

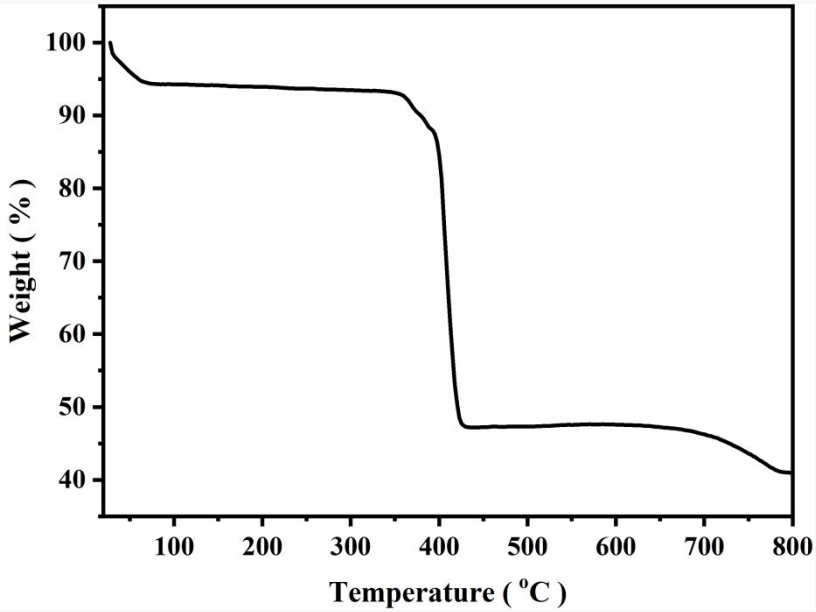

Figure S27. The TGA curve for 7.

7. UV-Vis spectra of 1-7.

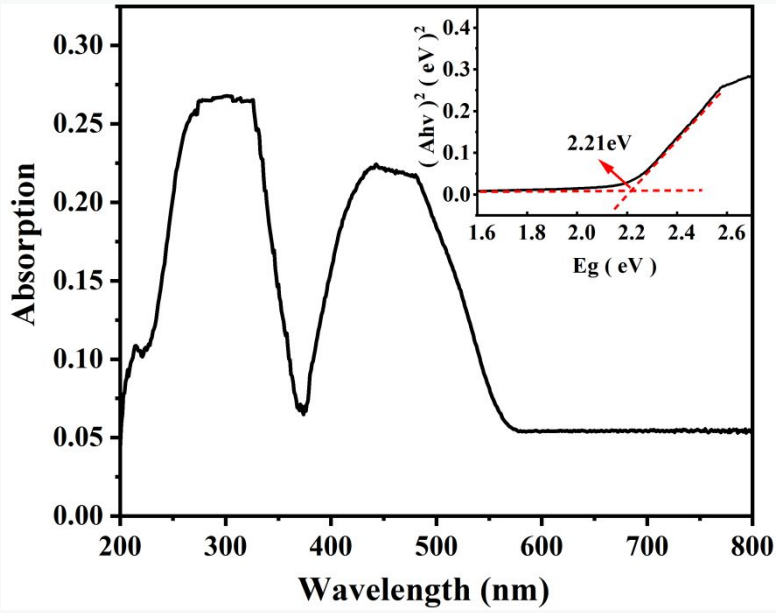

Fig S28. UV-Vis spectrum of 1.

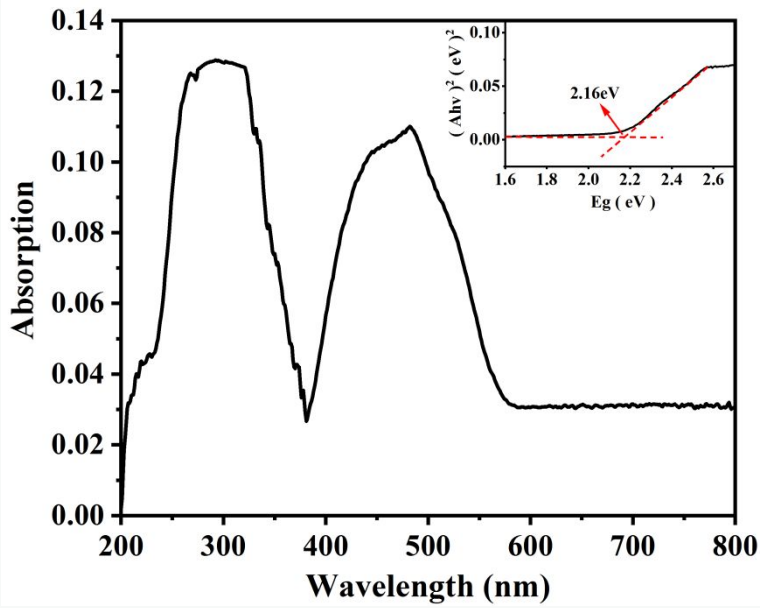

Fig S29. UV-Vis spectrum of 2.

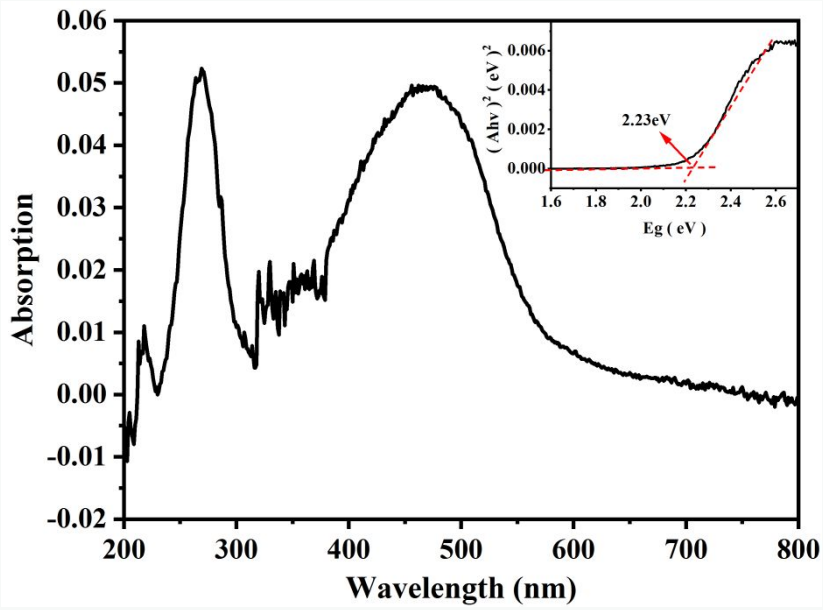

Fig S30. UV-Vis spectrum of 3.

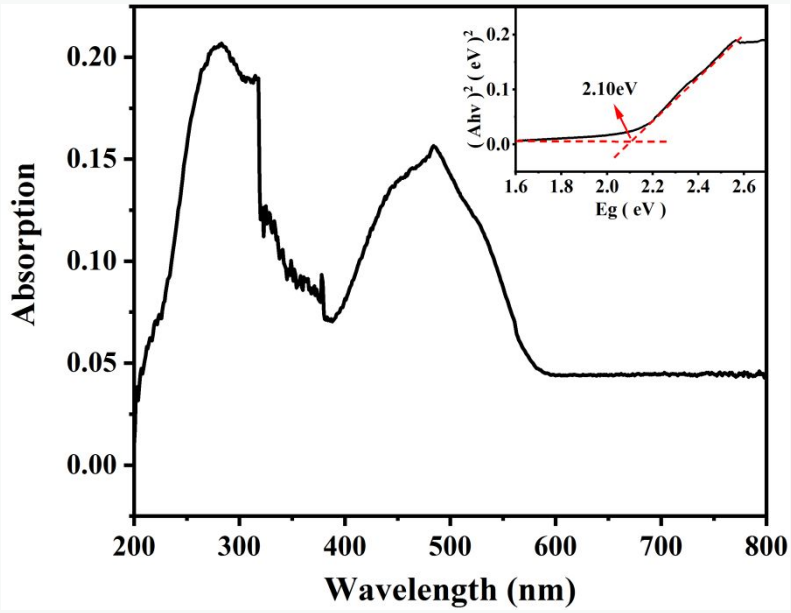

Fig S31. UV-Vis spectrum of 4.

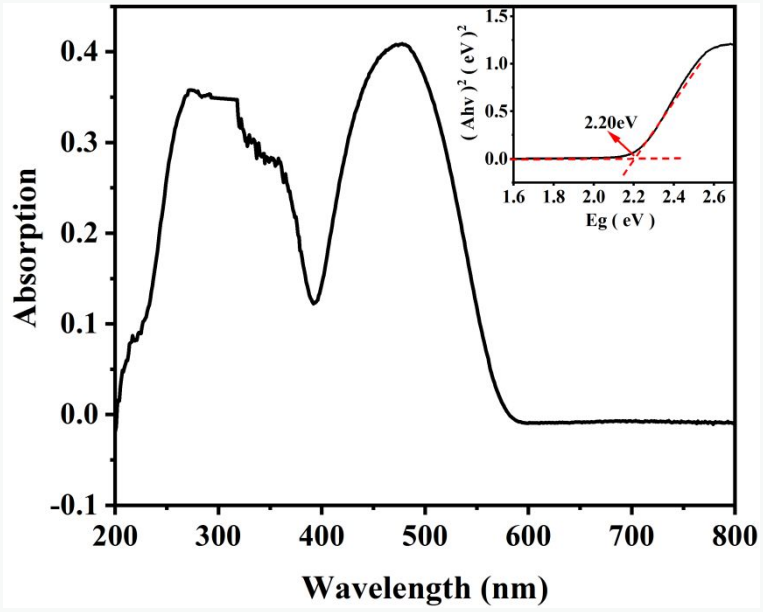

Fig S32. UV-Vis spectrum of 5.

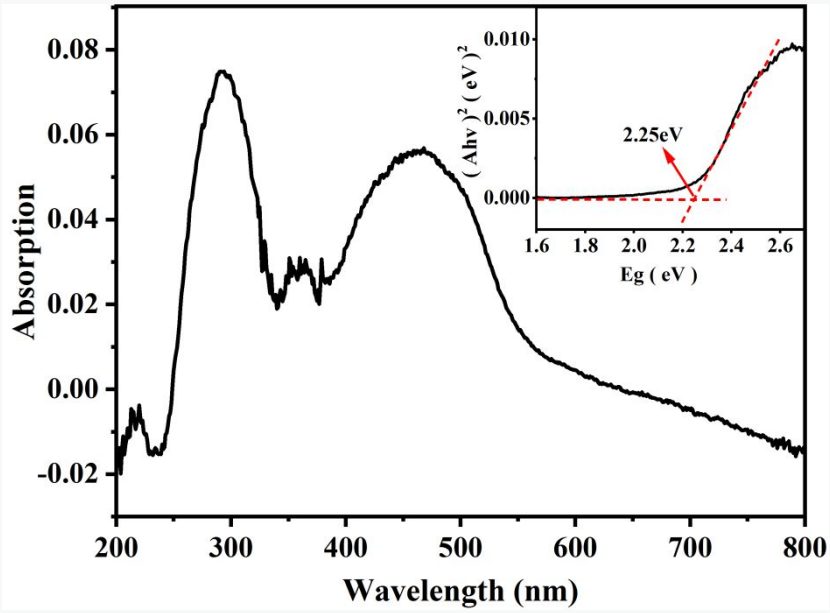

Fig S33. UV-Vis spectrum of 6.

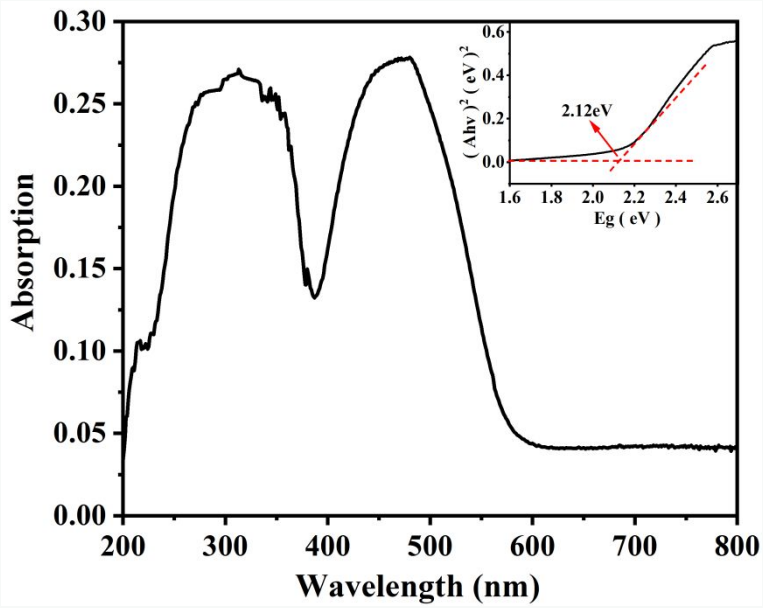

Fig S34. UV-Vis spectrum of 7.

8. Cyclic voltammetric curves of 1-7.

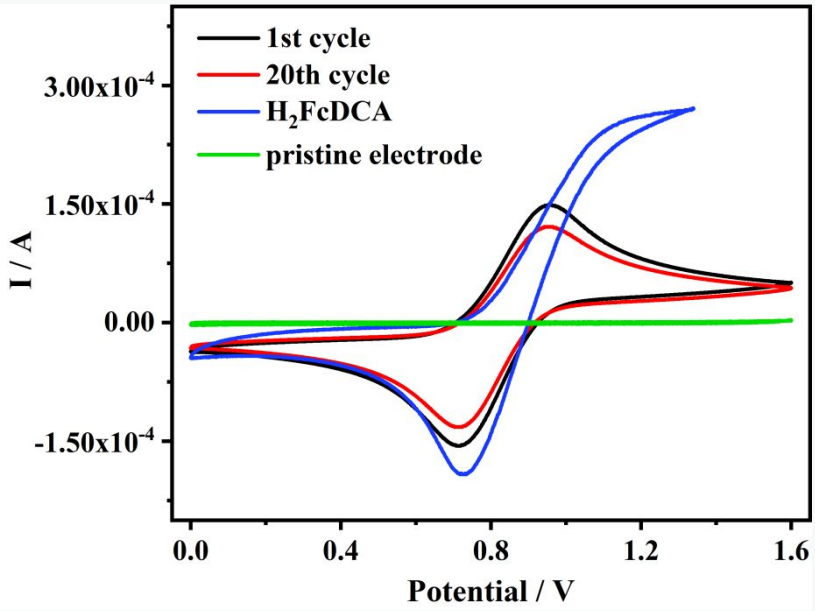

Figure S35. CV curves of 1 on a cleaned FTO glass (1.0 × 4.0 cm^2 , 50 Ω per square cm): first cycle (black) and 20th cycle (red) using a Pt plate as the counter electrode and an Ag/AgCl electrode as the reference electrode. For comparison, the curves of the pure FTO glass (green) and H_2FcDCA in solution (blue) are also shown.

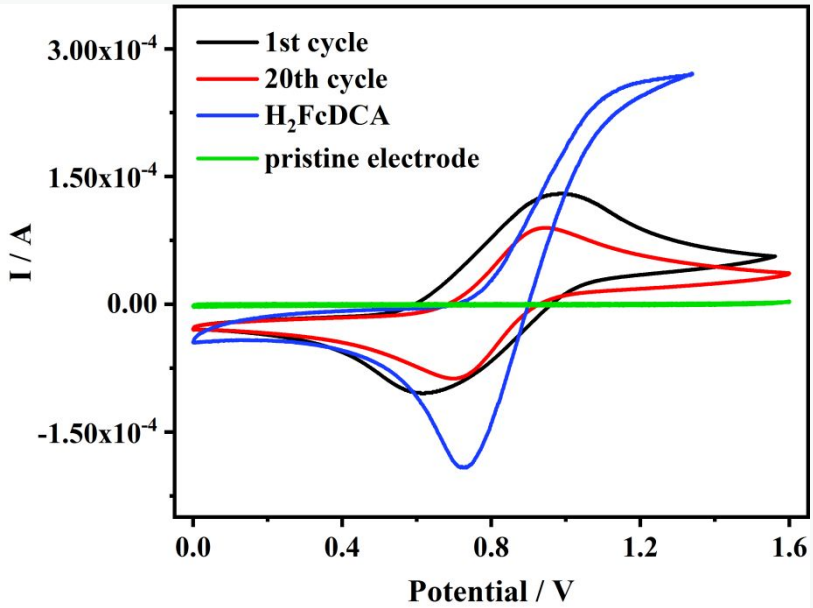

Figure S36. CV curves of 2 on a cleaned FTO glass (1.0 × 4.0 cm^2 , 50 Ω per square cm): first cycle (black) and 20th cycle (red) using a Pt plate as the counter electrode and an Ag/AgCl electrode as the reference electrode. For comparison, the curves of the pure FTO glass (green) and H_2FcDCA in solution (blue) are also shown.

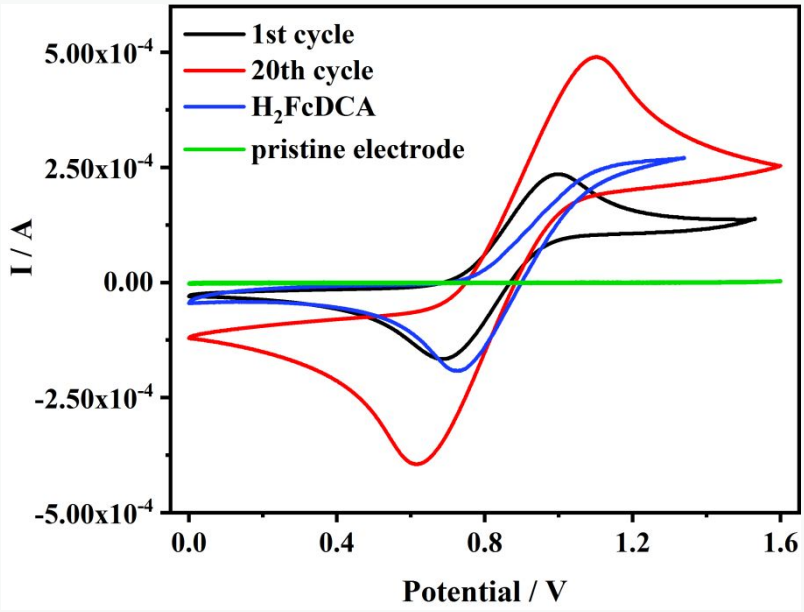

Figure S37. CV curves of 3 on a cleaned FTO glass (1.0 × 4.0 cm^2 , 50 Ω per square cm): first cycle (black) and 20th cycle (red) using a Pt plate as the counter electrode and an Ag/AgCl electrode as the reference electrode. For comparison, the curves of the pure FTO glass (green) and H_2FcDCA in solution (blue) are also shown.

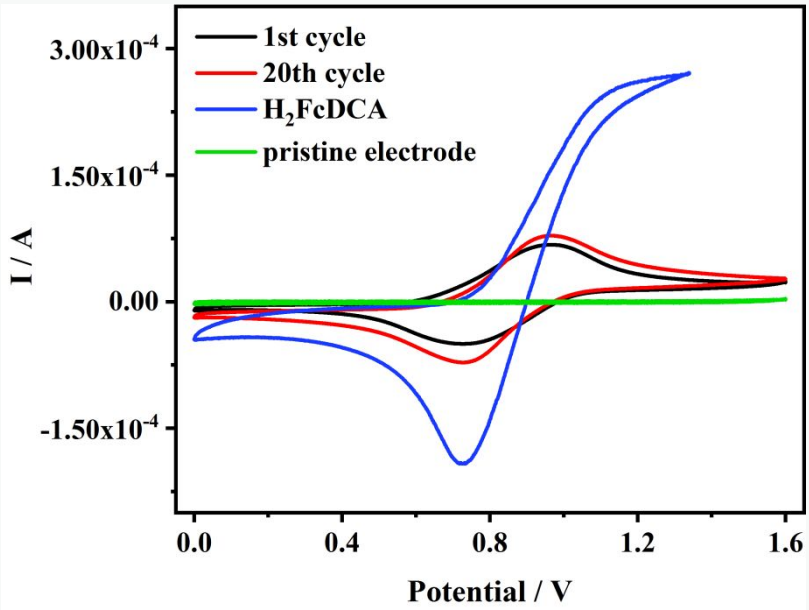

Figure S38. CV curves of 4 on a cleaned FTO glass (1.0 × 4.0 cm^2 , 50 Ω per square cm): first cycle (black) and 20th cycle (red) using a Pt plate as the counter electrode and an Ag/AgCl electrode as the reference electrode. For comparison, the curves of the pure FTO glass (green) and H_2FcDCA in solution (blue) are also shown.

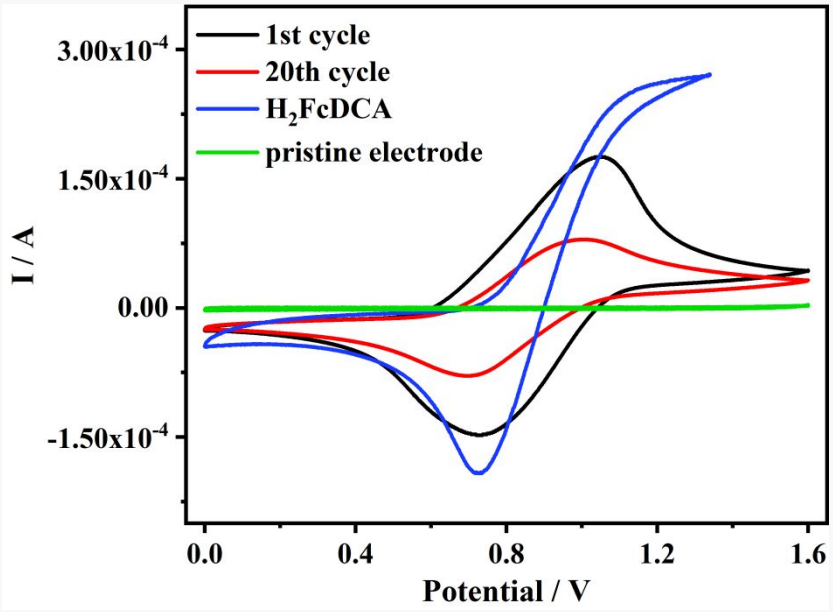

Figure S39. CV curves of 5 on a cleaned FTO glass (1.0 × 4.0 cm^2 , 50 Ω per square cm): first cycle (black) and 20th cycle (red) using a Pt plate as the counter electrode and an Ag/AgCl electrode as the reference electrode. For comparison, the curves of the pure FTO glass (green) and H_2FcDCA in solution (blue) are also shown.

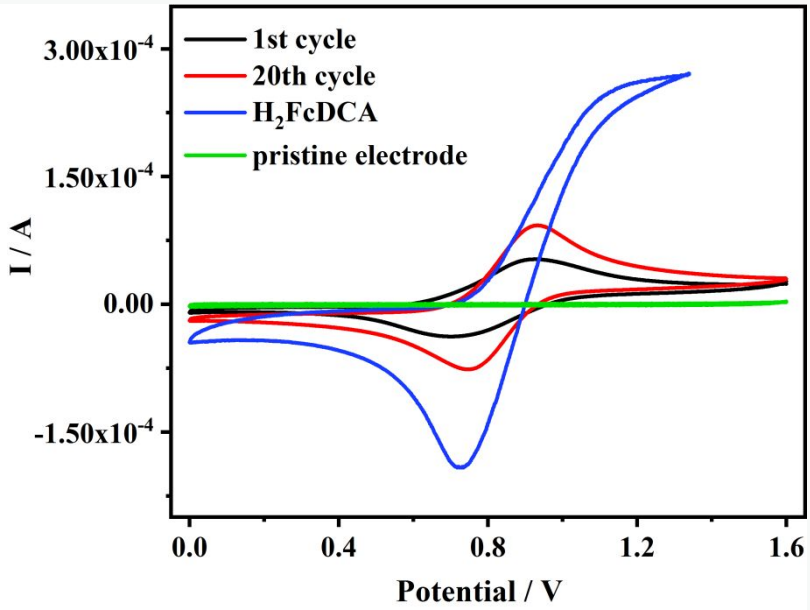

Figure S40. CV curves of 6 on a cleaned FTO glass (1.0 × 4.0 cm^2 , 50 Ω per square cm): first cycle (black) and 20th cycle (red) using a Pt plate as the counter electrode and an Ag/AgCl electrode as the reference electrode. For comparison, the curves of the pure FTO glass (green) and H_2FcDCA in solution (blue) are also shown.

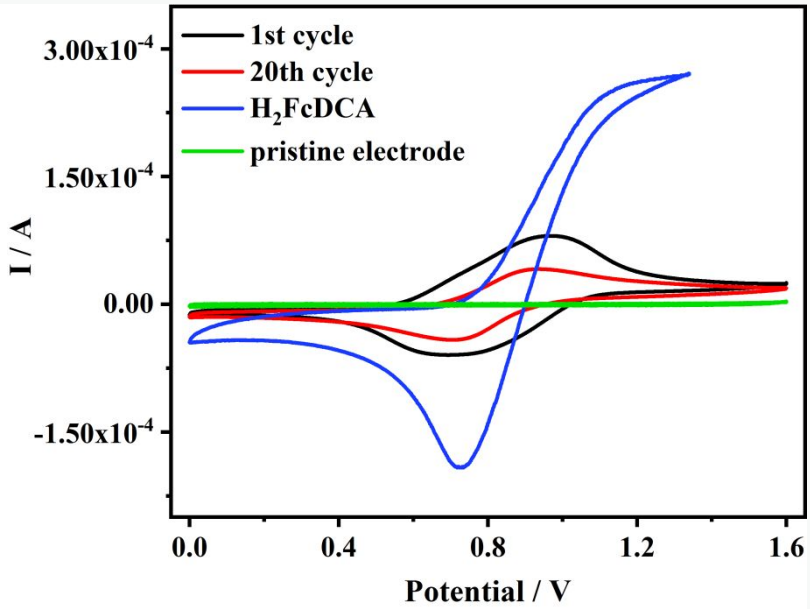

Figure S41. CV curves of 7 on a cleaned FTO glass (1.0 × 4.0 cm^2 , 50 Ω per square cm): first cycle (black) and 20th cycle (red) using a Pt plate as the counter electrode and an Ag/AgCl electrode as the reference electrode. For comparison, the curves of the pure FTO glass (green) and H_2FcDCA in solution (blue) are also shown.

9. Photocurrent responses of 1-7.

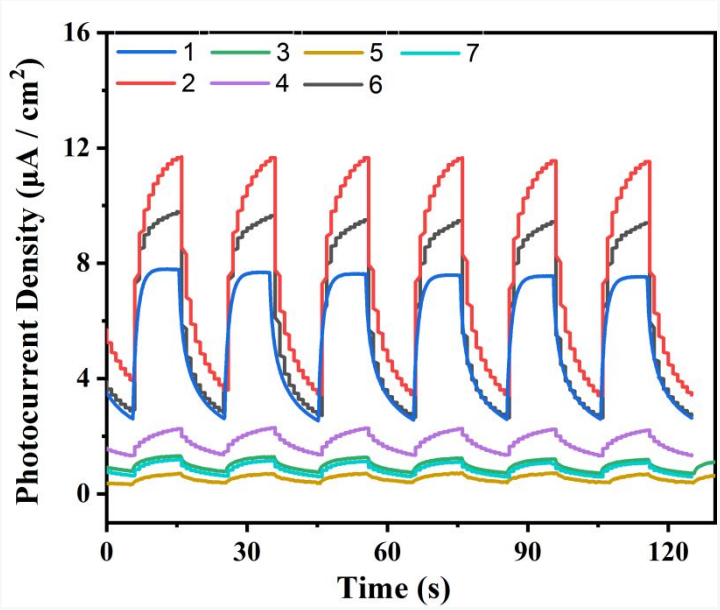

Fig S42. 0.4 V-bias photocurrent responses of electrodes derived from compounds 1-7 in a 0.2 M Na_2SO_4 aqueous solution under repetitive chopped visible light irradiation.

10. Gas adsorption experiments

Gas adsorption experiments with activation via supercritical drying.

The general supercritical drying method is performed according to the published procedures.[1] The sample 7 was activated with supercritical CO_2 in a Tousimis Samdri PVT-30 critical point dryer. Before drying, the sample 7 was thoroughly washed with anhydrous ethanol (EtOH) for three times then dried in air at room temperature. Then sample 7 was placed inside the dryer and was exchanged with CO_2 (Liquid) over a period of 8 h. During this time, the liquid CO_2 was vented under positive pressure for 5min each hour. The rate of venting of CO_2 (Liquid) was always kept below the rate of filling so as to maintain a full drying chamber. After 8h of venting and soaking with CO_2 (Liquid), the chamber was sealed and the temperature was raised to 30 °C. This brought the chamber pressure to around 90 bar, that is, above the critical point of CO_2. The chamber was vented over the course of 12–18h.

The isosteric heats of adsorption were calculated according to Clausius-Clapeyron equation[2]:

$$\frac{\partial(\ln P)}{\partial(1/T)} = -\frac{Qst}{R}$$

where Qst is the isosteric heats of adsorption, R is gas constant (8.314 $J \cdot mol^{-1} \cdot K^{-1}$).

Discussion: The pure component sorption isotherms of 7 for various hydrocarbons at 273 K and 298 K are also shown in Figure S43 and Figure S44. Compound 7 exhibits adsorption capacities to C_2H_2 (53.7 $cm^3\ g^{-1}$, 42.4 $cm^3\ g^{-1}$), C_2H_6 (43.0 $cm^3\ g^{-1}$, 32.4 $cm^3\ g^{-1}$), C_2H_4 (40.4 $cm^3\ g^{-1}$, 30.8 $cm^3\ g^{-1}$), and CH_4 (24.2 $cm^3\ g^{-1}$, 15.1 $cm^3\ g^{-1}$) at 273 K and 298K, respectively. The isosteric heats of adsorption (Qst) for 7 was calculated using the adsorption data collected at 273 K and 298 K. Virial analysis of the CO_2 adsorption isotherms revealed that the Qst of CO_2 at zero surface coverage is 12.40 kJ/mol (Figure S45). The Qst values of C_2H_2, C_2H_4, C_2H_6 and CH_4 adsorption were 12.30, 21.79, 8.26 and 32.54 kJ/mol, respectively (Figure S45). The Henry's constants were used to estimate the adsorption selectivity of 7 for C_2H_2, C_2H_4, C_2H_6 and CO_2 over CH_4. The calculated adsorption selectivity were 13.2, 14.6, 15.4 and 5.7 at 273 K, and 9.2, 13.7, 19.9 and 9.3

at 298K, correspondingly (Figure S46 and Figure S47).

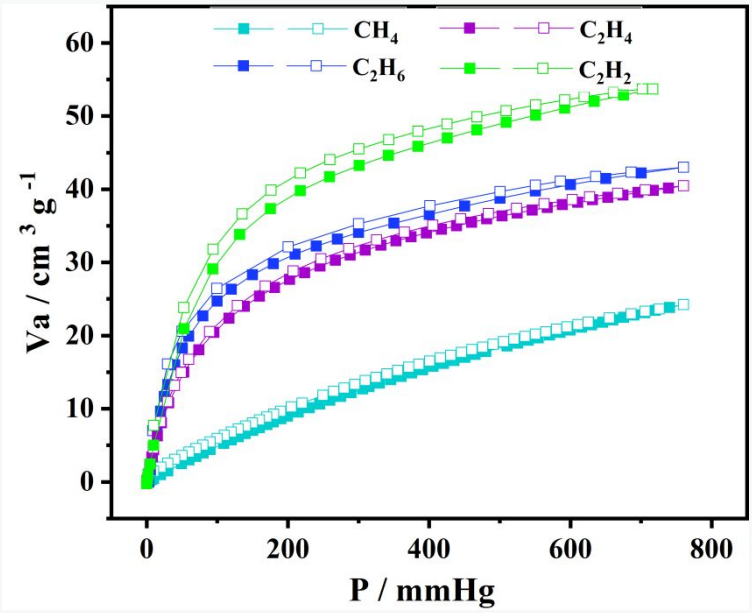

Fig S43. CH_4, C_2H_6, C_2H_4 and C_2H_2 adsorption isotherms of compound 7 at 273.15 K. Solid represents adsorption and open represents desorption.

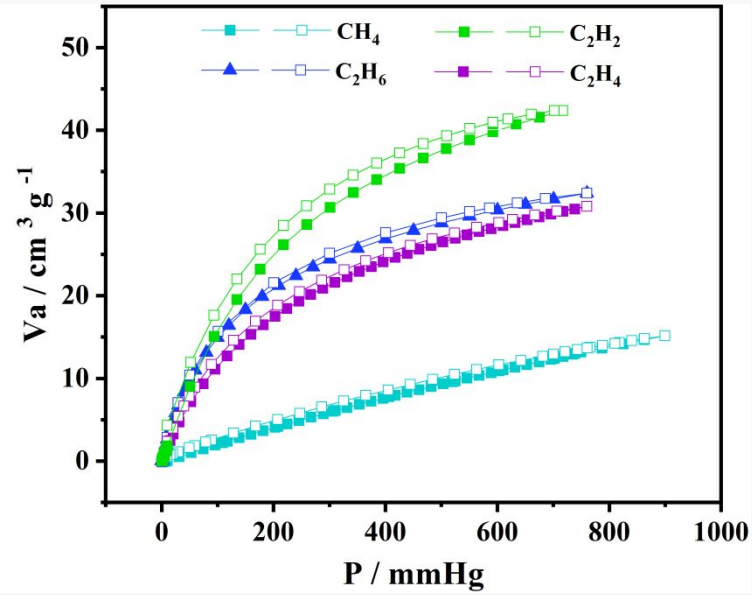

Fig S44. CH_4, C_2H_6, C_2H_4 and C_2H_2 adsorption isotherms of compound 7 at 298.15 K. Solid represents adsorption and open represents desorption.

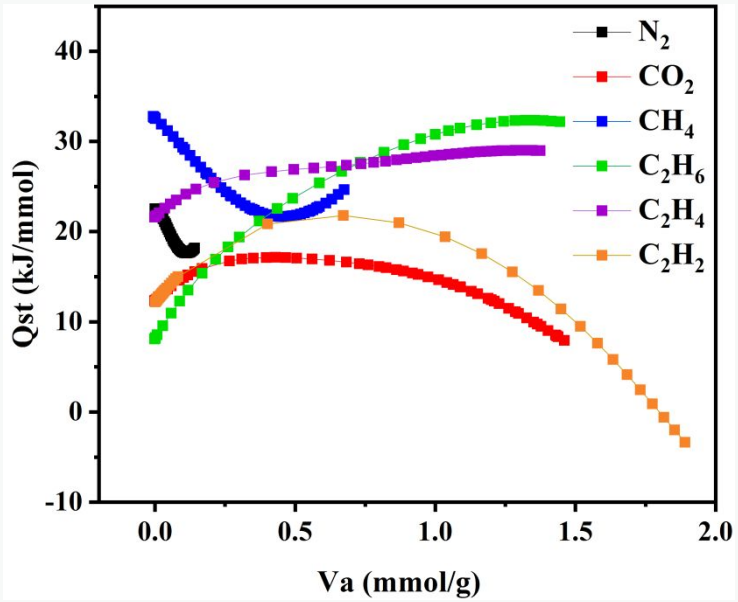

Figure S45. The isosteric heat of N_2, CO_2, CH_4, C_2H_6, C_2H_4 and C_2H_2 adsorption for 7 estimated by Clausius-Clapeyron equation.

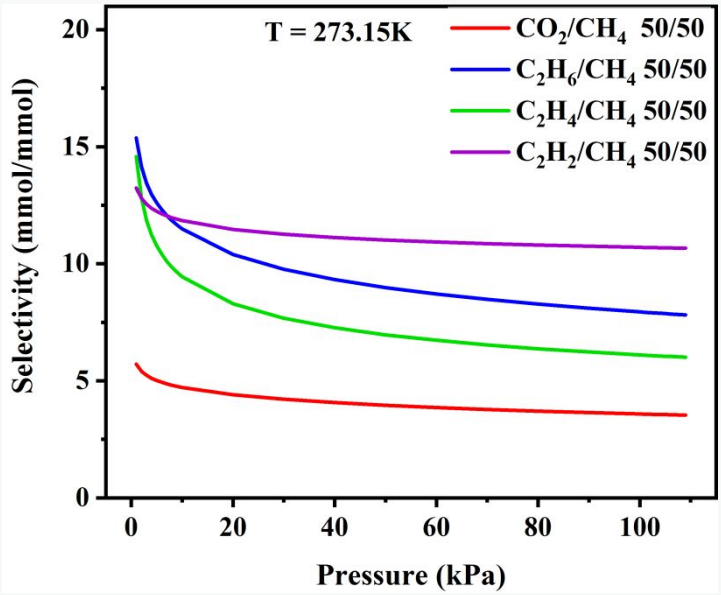

Figure S46. IAST-predicted adsorption selectivity of C_2/C_1, and CO_2/CH_4 on 7 at 298.15 K (C_2/C_1 equimolar binary mixtures).

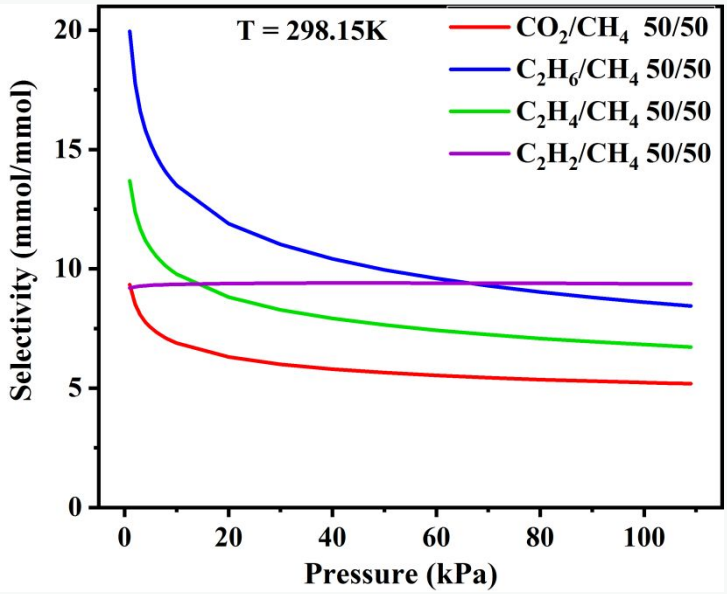

Figure S47. IAST-predicted adsorption selectivity of C_2/C_1, and CO_2/CH_4 on 7 at 298.15 K (C_2/C_1 equimolar binary mixtures).

References

(1) Nelson, A. P.; Farha, O. K.; Mulfort, K. L.; Hupp, J. T. Supercritical Processing as a Route to High Internal Surface Areas and Permanent Microporosity in Metal-Organic Framework Materials. *J. Am. Chem. Soc.* **2009,** *131*, 458-560.

(2) Rowsell, J. L. C.; Yaghi, O. M. Effects of functionalization, catenation, and variation of the metal oxide and organic linking units on the low-pressure hydrogen adsorption properties of metal-organic frameworks. *J. Am. Chem. Soc.* **2006,** *128*, 1304-1315.